Monthly Notices of the ROYAL ASTRONOMICAL SOCIETY

MNRAS **524,** 5944–5953 (2023) https://doi.org/10.1093/mnras/stad2252
Advance Access publication 2023 July 27

Density streams in the disc winds of Classical T Tauri stars

P. P. Petrov [1]★ K. N. Grankin [1] E. V. Babina,[1] S. A. Artemenko,[1] M. M. Romanova,[2]★ S. Yu. Gorda,[3] A. A. Djupvik [4,5] and J. F. Gameiro [6,7]

[1]*Crimean Astrophysical Observatory, p/o Nauchny, 298409, Republic of Crimea*
[2]*Cornell University, Ithaca, NY 14853, USA*
[3]*Ural Federal University, 51, Lenin av., Ekaterinburg 620000, Russia*
[4]*Nordic Optical Telescope, Rambla José Ana Fernández Pérez, 7, E-38711 Breña Baja, Spain*
[5]*Department of Physics and Astronomy, Aarhus University, Ny Munkegade 120, DK-8000 Aarhus C, Denmark*
[6]*Instituto de Astrofísica e Ciências do Espaço, Universidade do Porto, CAUP, Rua das Estrelas, P-4150-762 Porto, Portugal*
[7]*Departamento de Física e Astronomia, Faculdade de Ciências, Universidade do Porto, Rua do Campo Alegre 687, P-4169-007 Porto, Portugal*

Accepted 2023 July 21. Received 2023 July 21; in original form 2023 February 27

ABSTRACT

Spectral and photometric variability of the Classical T Tauri stars RY Tau and SU Aur from 2013 to 2022 is analysed. We find that in SU Aur the H α line's flux at radial velocity RV $= -50 \pm 7$ km s^{-1} varies with a period P $= 255 \pm 5$ d. A similar effect previously discovered in RY Tau is confirmed with these new data: $P = 21.6$ d at RV $= -95 \pm 5$ km s. In both stars, the radial velocity of these variations, the period, and the mass of the star turn out to be related by Kepler's law, suggesting structural features on the disc plane orbiting at radii of 0.2 au in RY Tau and 0.9 au in SU Aur, respectively. Both stars have a large inclination of the accretion disc to the line of sight – so that the line of sight passes through the region of the disc wind. We propose there is an azimuthal asymmetry in the disc wind, presumably in the form of 'density streams,' caused by substructures of the accretion disc surface. These streams cannot dissipate until they go beyond the Alfven surface in the disc's magnetic field. These findings open up the possibility to learn about the structure of the inner accretion disc of CTTS on scales less than 1 au and to reveal the orbital distances related to the planet's formation.

Key words: stars: individuals: RY Tau, SU Aur – stars: variables: T Tauri, Herbig Ae/Be – stars: winds, outflows.

1 INTRODUCTION

The Classical T Tauri Stars (CTTSs) are commonly recognized as the counterparts of the young Sun, allowing us to study the Solar system's past evolution. The formation of a planetary system around a young star occurs simultaneously with the formation of the star itself – when the central star and the surrounding protoplanetary disc are still hidden from the observer by the gas-dust shell (Nixon, King & Pringle 2018). By the time we see a star as a CTTS, there are already possible indirect signatures of planets in the surrounding disc. However, detecting these planets is quite difficult. The classical method of precision measurements of radial velocities is hardly applicable for CTTSs: as a result of magnetospheric accretion, hotspots form on the stellar surface, distorting the photospheric spectrum (e.g. Petrov et al. 2011). Unlike long-lived cool spots, these hot spots can change on a time-scale of a few days, resulting in jittering the measured radial velocity. Although thousands of exoplanets are currently discovered and their properties and migrations are being investigated, we still have very limited information about planets around CTTSs (see Grandjean et al. 2021 and references therein).

In this article, we consider the possibility of detecting emerging planets in the inner accretion disc by their influence on the disc wind.

★ E-mail: petrov@craocrimea.ru (PPP); marinaromanova55@gmail.com (MMR)

The wind properties in CTTS are usually inferred from the kinematics of spatially unresolved, blueshifted forbidden emission lines including [O I], [S II], [N II], [Fe II], [Ne II], as well as P Cygni profiles in strong permitted emission lines, such as He I 10 830 Å (see review by Pascucci et al. 2022 and references therein). Analysis of the FUV spectra of CTTS showed that the mass-loss is concentrated in the innermost region of the disc, < 1–2 au (Xu et al. 2021).

In the visible spectral region, the most obvious signature of the wind is the variable blue-shifted depression in the H α emission profile. The radial velocity of the blue-shifted depression depends on the wind velocity and the inclination angle of the disc axis to the line of sight.

However, when observing the variability of the H α line formed in the CTTS wind, it is difficult to identify the type of wind responsible for the changes in the line profile. Different types of outflow can start at the boundary between the stellar magnetosphere and the inner accretion disc. The disc wind, accelerated by the magnetocentrifugal force, emanates from the disc surface (Blandford & Payne 1982). Besides, the X-wind (Shu et al. 2016), conical wind (Romanova et al. 2009; Kurosawa & Romanova 2012), magnetospheric ejections (Zanni & Ferreira 2013), and magnetic propeller were discussed (see Romanova & Owocki 2015; Romanova et al. 2018 for review).

Emission-line profiles provide information about the dynamics of gas flows around a CTTS. The formation of various types of the H α emission profiles in spectra of CTTS was considered by Kurosawa, Harries & Symington (2006) within models of the magnetosphere

Table 1. The basic parameters of SU Aur and RY Tau.

Star	Sp. type	$T_{\rm eff}$ K	$R/R_\odot$	$L/L_\odot$	$M/M_\odot$	$\dot{M}$ 10^{-8} $M_\odot$ yr^{-1}	Inner disc inclination (deg)
SU Aur	G1	5945	2.6 ± 0.4	7.8 ± 1.2	1.7 ± 0.2	$0.5 - 0.6(\pm 0.4)$	50.9 ± 1
RY Tau	G1	5945	2.9 ± 0.4	9.6 ± 0.5	2.0 ± 0.3	$6.4 - 9.1(\pm 4.9)$	60.0 ± 1

Notes. Stellar parameters: Calvet et al. (2004).
Inner disc inclinations: Labdon et al. (2019, SU Aur) and Perraut, Gravity & Collaboration (2021, RY Tau).

and the disc wind. They have shown that at a sufficiently high inclination angle of the line of sight, the main feature in the spectral line is blue-shifted absorption due to the disc wind. A similar result has been obtained while modelling the disc wind in the He I (10830) spectral line (Kurosawa, Romanova & Harries 2011).

Models of H α line profiles formed in the magnetosphere and the disc wind of CTTSs were calculated and compared with the observed ones (Kurosawa et al. 2011; Tambovtseva, Grinin & Weigelt 2014).

Variability of spectral-line profiles caused by the gas flows, including the outflows from the boundary between the magnetosphere and the accretion disc, is well documented for some CTTS, e.g. by Sousa et al. (2021, V2129 Oph), Alencar et al. (2018, LkCa15), Bouvier et al. (2007b, AA Tau), Bouvier et al. (2023, GM Aur), while less is known about variations in the disc wind.

There is a class of young stars – FUors, where the disc wind dominates over other types of outflow. The prototype of the class, FU Ori, is a low-mass CTTS with the mass-loss rate in the disc wind 2×10^{-4} $M_\odot$ yr^{-1} (Zhu et al. 2007), while in a CTTS the average value is 10^{-9} $M_\odot$ yr^{-1} (Bouvier et al. 2007a). Herbig, Petrov & Duemmler (2003) analysed a series of spectra of FU Ori, obtained in 1997–1999. They found that the intensity of the P Cyg absorption in the H α line varied with a period of 14.8 d. A decade later, Powell et al. (2012) analysed their series of spectral observations of FU Ori of 2007. They confirmed the existence of the periods and refined its values: 13.5 d. The case of FU Ori shows that periodic variations in the disc wind are real and worth to be investigated.

A long time series of spectroscopic observations of a CTTS may potentially reveal rotationally modulated variations in the wind density at certain radial velocities. Such a Doppler probe may provide information about the inner disc structure. In this article, we focus on time variability of H α line fluxes at different radial velocities across the broad-line profile.

We present the results of spectral and photometric monitoring of RY Tau and SU Aur, both with large inclinations, so that line of sight intersects the region of the disc winds. The stars are bright, and each has been explored in detail before. The stellar parameters, according to Calvet et al. (2004), are presented in Table 1. The stars are relatively massive and may be classified as the intermediate objects between the CTTS and the HAeBe stars.

Our programme of spectroscopic and photometric monitoring of RY Tau were started in 2013, then later in 2015 another object, SU Aur, was included. The first results of this program were published in Petrov et al. (2019), hereafter referred as Paper I: from analysis of the variable outflow velocity and the circumstellar extinction of RY Tau we found that the obscuring dust is near the star, at the dust sublimation radius of about 0.2 au. During events of enhanced outflow, the circumstellar extinction becomes lower. As more data on RY Tau accumulated, we found another effect: the spectral indicators of the accretion and outflows (in H α and Na I lines) vary with a period of about 22 d. The infall and outflow vary in antiphase: an increase of infall is accompanied by a decrease of outflow, and vice versa. We considered two possible interpretations: (1) quasi-periodic magnetohydrodynamics processes at the disc-magnetosphere boundary in the propeller mode, or (2) a massive planet on inclined orbit in the accretion disc (Petrov et al. 2021).

By now we have accumulated nine seasons of observation of RY Tau and seven seasons of SU Aur, including high-resolution spectroscopy and photometry. In this paper, we investigate variability of the H α profile in spectra of RY Tau and SU Aur, with the aim to confirm the periodic variations and find their possible relationship with the structure of the accretion disc and the disc wind.

The paper is organized as follows. In Section 2, we overview the basic properties of RY Tau and SU Aur. In Section 3, we address briefly the instruments and observation sites. Then, in Section 4 we analyse the variability of brightness and H α line fluxes in RY Tau and SU Aur. The major part is devoted to the frequency analysis of variability of the H α line flux at different radial velocities. Finally, in Section 5 we discuss the results in terms of the disc wind axial asymmetry and the accretion disc structures.

2 BASIC PROPERTIES OF RY TAU AND SU AUR

RY Tau and SU Aur are young stars with emission-line spectra, showing signatures of outflows and accretion. Both stars possess accretion discs. Excess continuous radiation is present in the far UV spectrum of both stars, larger in RY Tau than in SU Aur. The mass accretion rates (Table 1) were estimated from the accretion luminosities in the UV spectrum (Calvet et al. 2004).

Inclinations of the *inner* disc were derived from *K*-band interferometry: $60^\circ \pm 1^\circ$ in RY Tau (Perraut et al. 2021) and $50.9^\circ \pm 1^\circ$ in SU Aur (Labdon et al. 2019). The inclination of the *outer* disc of RY Tau, as derived from ALMA observations, is $65^\circ \pm 0.1^\circ$ (Long et al. 2019). *K*-band interferometry of RY Tau by Davies et al. (2020) indicated that the central star is occulted by the disc surface layers close to the sublimation rim. They suggested that the aperiodic photometric variability of RY Tau is likely related to temporal and/or azimuthal variations in the structure of the disc surface layers.

Interferometric and polarimetric observations of SU Aur revealed more complicated structures with several dust tails connected to the Keplerian disc, indicating that late accretion events can still occur (Akiyama et al. 2019; Ginski et al. 2021).

Both stars are rapid rotators. In RY Tau, $v \sin i = 52 \pm 2$ km s^{-1} (Bouvier 1990; Petrov et al. 1999). The period of axial rotation was not detected directly either in photometric data or in variations of spectral line profiles. Assuming the inclination of the stellar rotational axis $i = 60^\circ$ (the same as in the accretion disc), stellar radius 2.9 ± 0.4 $R_\odot$ and $v \sin i = 52$ km s^{-1}, the expected period of the axial rotation may be about 3 d.

In SU Aur, $v \sin i = 60-66$ km s^{-1} (Nguyen et al. 2012). The period of axial rotation within 2.7−3.0 d was estimated from variations in emission-line profiles (Giampapa et al. 1993; Johns & Basri 1995) and in the red-shifted absorptions of He I and Balmer lines (Petrov et al. 1996).

Table 2. Reported periods in photometric and spectroscopic observations of SU Aur and RY Tau.

Star	Period (d)	Method	Year of obs.	Reference
SU Aur	1.55; 2.73	phot	1985–1986	1
	∼1.7	phot	1995–1999	2
	2.661	phot	2009–2010	3
	2.98	spec	1986–1990	4
	3.0	spec	1986–1992	5
	3.0	spec	1990–1994	6
	2.742	spec	1993–1994	7
	18.7	phot	1981–1991	8
RY Tau	20; 29.4	phot	1993, 1996	9
	23	spec	1975–1985	10
	21.6	spec	2013–2021	11

References: 1 – Herbst et al. (1987), 2 – DeWarf et al. (2003), 3 – Cody et al. (2013), 4 – Giampapa et al. (1993), 5 – Johns & Basri (1995), 6 – Petrov et al. (1996), 7 – Strassmeier et al. (1997), 8 – Gahm et al. (1993), 9 – Zajtseva (2010), 10 – Ismailov et al. (2015), 11 – Petrov et al. (2019, 2021).

RY Tau has an extended jet with a few knots of young dynamical ages (St-Onge & Bastien 2008; Agra-Amboage et al. 2009; Skinner, Audard & Guedel 2011). The jet is wiggled, which may indicate the presence of an unseen planetary or substellar companion to the star (Garufi et al. 2019). Interferometric images of the protoplanetary disc around RY Tau at millimetre wavelengths did not reveal planets more massive than 5 M_J at distances between 10 and 60 au (Isella, Carpenter & Sargent 2010).

Both RY Tau and SU Aur are irregular variables with long photometric records (Herbst & Stine 1984; Herbst et al. 1994; Zajtseva et al. 1996). No stable periods in the light variations were recorded, although quasi-periodic variations on different time-scales were reported by observers. The most extended series of photometric observations of RY Tau from 1965 to 2000 were analysed by Zajtseva (2010): periods of 20.0 and 29.4 d were revealed in the data of 1993 and 1996, respectively, and interpreted as probably caused by inhomogeneities in the circumstellar disc. A period of about 23 d in variations of emission-line intensities in UV and optical spectrum of RY Tau was reported by Ismailov, Adigezalzade & Bahaddinova (2015) and interpreted as due to protostellar objects orbiting in the inner accretion disc.

The light curve of SU Aur is characterized by a nearly constant maximum brightness level with a usually small amplitude of variability but interrupted at times by deep fading episodes (Grankin et al. 2007). Searches for periodic photometric variations gave conflicting results. Various authors reported finding different periods: 1.76 d (DeWarf et al. 2003), 1.55 or 2.73 d (Herbst et al. 1987), 2.7 d (Strassmeier et al. 1997), or their absence (Percy et al. 2006; Artemenko, Grankin & Petrov 2012). Only analysis of intense space observations performed on the MOST satellite made it possible to reliably detect a low-amplitude periodic process (2.661 d) against the background of a longer and higher amplitude brightness change (Cody et al. 2013).

All the reported periods in photometric and spectroscopic observations of SU Aur and RY Tau are summarized in Table 2. More detailed review of the previously reported photometric periods in SU Aur was presented in Cody et al. (2013). In summary, the short periods (<3 d) in SU Aur indicate the axial rotation of the star, while the longer periods observed in RY Tau are probably related to rotations of the inner region of the accretion disc. A more detailed overview of the basic properties of RY Tau and SU Aur was presented in Paper I.

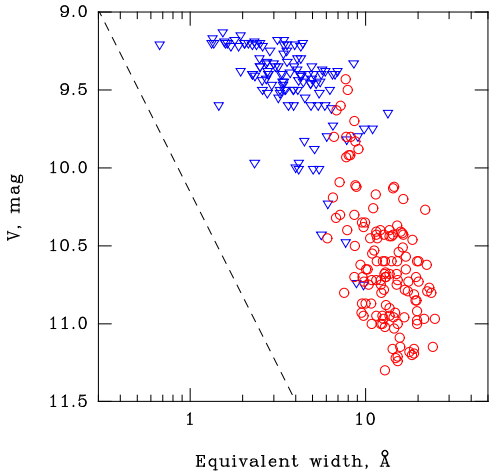

Figure 1. Equivalent width of the H α emission as a function of stellar brightness in SU Aur (blue triangles) and RY Tau (red circles).

3 OBSERVATIONS

A major part of our spectral data was obtained with an echelle spectrograph at the 2.6 m Shajn reflector of the Crimean Astrophysical Observatory (CrAO) and with a fibre-fed echelle spectrograph at the 1.21-m telescope of Kourovka Observatory of the Ural Federal University. The spectral resolutions $\lambda/\Delta\lambda$ were 27 000 and 15 000 correspondingly. Two spectral orders, including H α and D Na I lines, were extracted from the echelle frame for analysis. The Crimean observations were carried out in short time series by 4–6 consequent nights every month since September to March, in each season. The spectral regions including H α and D Na I lines were registered.

In one season, 2015–2016, multisite monitoring of RY Tau and SU Aur was performed, including observations with the ALFOSC grism spectrograph at the 2.56-m Nordic Optical Telescope ($\lambda/\Delta\lambda =$ 15000), and the CAFE echelle spectrograph at the 2.2-m telescope at Centro Astronomico Hispano-Aleman (CAHA), $\lambda/\Delta\lambda = 30000$. More information about the observations and data reductions was presented in our previous publication (Paper I).

As the data from our monitoring of these stars accumulated, the results obtained were published by Petrov et al. (2019, 2021). At present, our data set contains 193 spectra (193 nights) of RY Tau and 176 spectra of SU Aur, suitable for analysis of H α line variability. There are fewer spectra of the absorption D Na I lines, suitable for analysis, since these lines are noisy on nights with poor image quality, and often contaminated with atmospheric water lines. On most of the nights of spectral observations, *BVR* photometry of both targets was carried out at a 1.25 m telescope at CrAO. The log of spectral observations and the *V*-magnitudes for the dates of observations are presented in Tables A1 and A2 in the same format as in the Paper I.

In the next section, we analyse the H α line profile variability in the whole set of data obtained in 2013–2022: nine seasons of RY Tau and seven seasons of SU Aur.

4 RESULTS

In both stars, RY Tau and SU Aur, the equivalent width of the H α emission increases as the star gets weaker (Fig. 1). This effect is caused by the circumstellar dust which obscures the star, but not the whole region radiating in H α line. The straight line in Fig. 1 indicates the slope expected for the case of constant H α flux at variable stellar

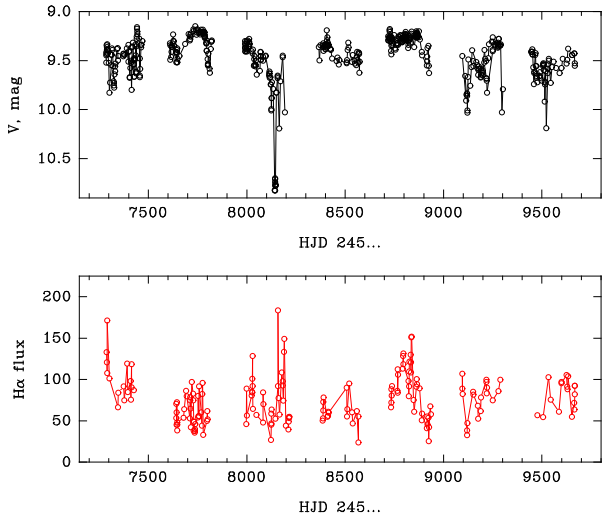

Figure 2. Light curve (above) and H α flux variations (below) of SU Aur in 2015–2022. The H α flux is expressed in units 3.67 $\times$ 10^{-13} erg cm^{-2} s^{-1}.

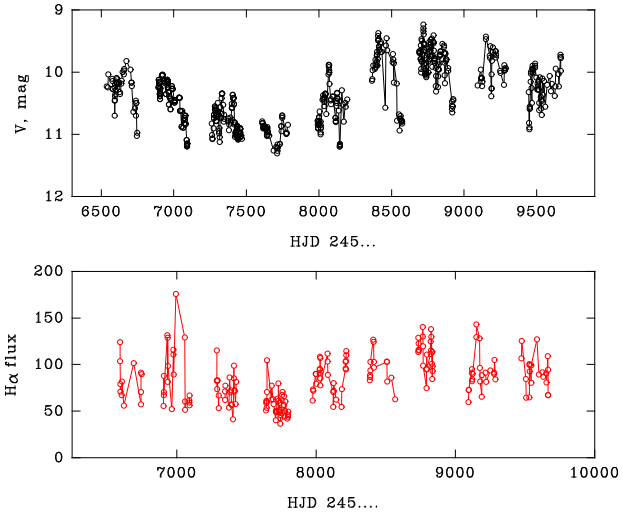

Figure 3. Light curve (above) and H α flux variations (below) of RY Tau in 2013–2022. The H α flux units: 3.67 $\times$ 10^{-13} erg cm^{-2} s^{-1}.

continuum. The observed scatter of H α equivalent widths is due to the intrinsic variability of the H flux.

Figs 2 and 3 show stellar brightness and H α flux variability in SU Aur and RY Tau according to our observations, presented in Tables A1 and A2. The H α flux is calculated as F = EW $\times$ $10^{-0.4(V-10)}$, where the line flux is expressed in units of the continuum flux density of a star with V = 10 mag, which is 3.67 $\times$ 10^{-13} erg cm^{-2} s^{-1}. The magnitudes in the R band would be more appropriate for this conversion, but only V magnitudes are available to cover the full set of spectroscopic data. However, we have checked that for RY Tau the colour $V - R$ does not change considerably with brightness: on average, $V - R$ = 1.1 $\pm$ 0.1. In the case of SU Aur, the probable error in the H α flux, caused by variations in the $V - R$ colour, is about 5 per cent, while the H α flux varies by a factor of 3 and more (see Fig. 2).

For analysis of spectral line profiles, the spectra obtained at different instruments were re-binned to get a common sampling of the wavelength scale. In the following analysis of H α line profile variations, we use the astrocentric radial velocity scale, assuming that

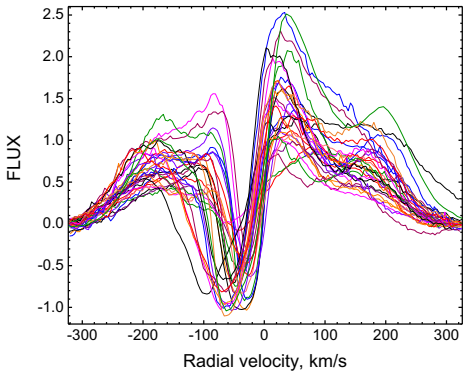

Figure 4. A sample of H α line profile variability in SU Aur.

the radial velocity of RY Tau and SU Aur is +18 km s^{-1} (Petrov et al. 1996, 1999). Radial velocities variations due to possible photospheric inhomogeneities (spots) are expected to be less than a few km s^{-1}. A spot would also result in rotational modulation of stellar brightness. This effect was not found in RY Tau but may have been observed in SU Aur (see Table 2).

4.1 H α profile variability in SU Aur

A sample of 30 H α profiles in SU Aur, observed in different seasons of 2015–2022, is presented in Fig. 4 to show the pattern and amplitude of the line profile variability, typical for this star. All the 176 H α spectra were used to quantify the line profile variability.

A power spectrum of the flux variations was calculated in each radial velocity bin across the H α line profile. This results in a two-dimensional (2D) periodogram in the space 'frequency versus radial velocity,' which reveals the areas of probable periodic signals. The power spectra were calculated following the procedure CORRELOGRAM described in S. Lawrence (1987). For better visibility of the area of a periodic signal, the power spectra were smoothed to a lower frequency resolution, about 10^{-3} d^{-1}. The 2D periodogram of the Hα line flux is shown in Fig. 5. The power of the periodic oscillations is colour coded from blue to red as it increases. Most of the power is concentrated in the bluewards of H α at low frequencies. This region of the periodogram is expanded in the lower part of Fig. 5. The most significant period P = 255 $\pm$ 5 d ($1/P$ = 0.004) is at a radial velocity RV = $-$45 $\pm$ 7 km s^{-1}. The same result was obtained when only high-resolution ($R \geq$ 27 000) spectra were used in the analysis.

The period of 255 d is seen also in the ratio of fluxes measured at $-$50 and +25 km s^{-1}, corresponding to the deepest absorption and the highest emission in the profile. This ratio may be considered as a parameter of the H α profile asymmetry. The power spectrum and convolution of this parameter with a period of 255 d are presented in Fig. 6. The first and the second halves of the time series (2015–2018 and 2019–2022, respectively) are displayed with different symbols, to show that periodic variations persisted throughout the whole data set. The same period is also present in the intensity variations of the blue-shifted absorptions in the D Na I lines.

4.2 H α profile variability in RY Tau

A sample of 30 H α profiles in RY Tau, observed in different seasons between 2018 and 2021, is presented in Fig. 7 showing the pattern and amplitude of the profile variability, typical for this star. All the 193 H α spectra were used to quantify the line profile variability.

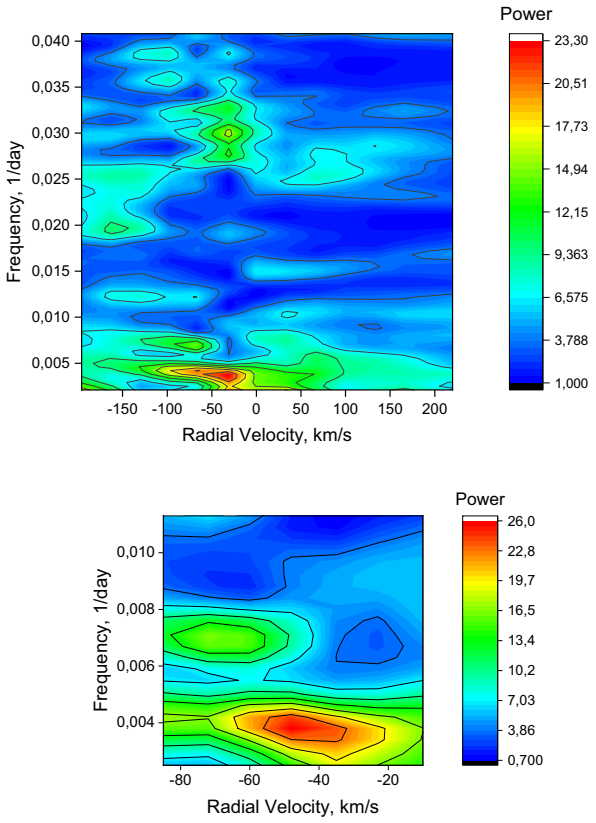

Figure 5. Upper: Two-dimensional periodogram of the H α line flux in SU Aur. Lower: enlarged fragment of the periodogram. The red spot indicates the area of the most powerful oscillations with a period of 255 $\pm$ 5 d.

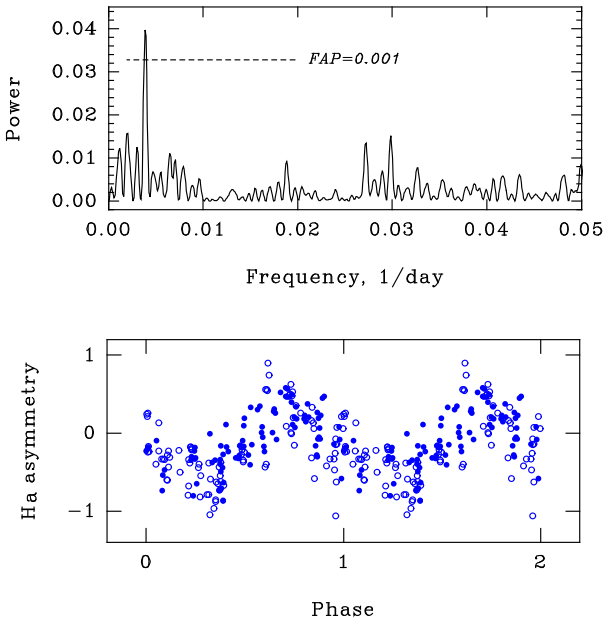

Figure 6. Top panel: Power spectrum of the H α profile asymmetry in SU Aur. Bottom panel: H α profile asymmetry, convolved with the period P = 255 d. Dots and circles correspond to the first and the second halves of the time series, correspondingly.

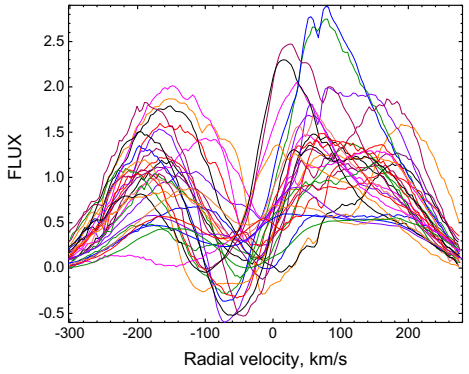

Figure 7. A sample of H α line profile variability in RY Tau.

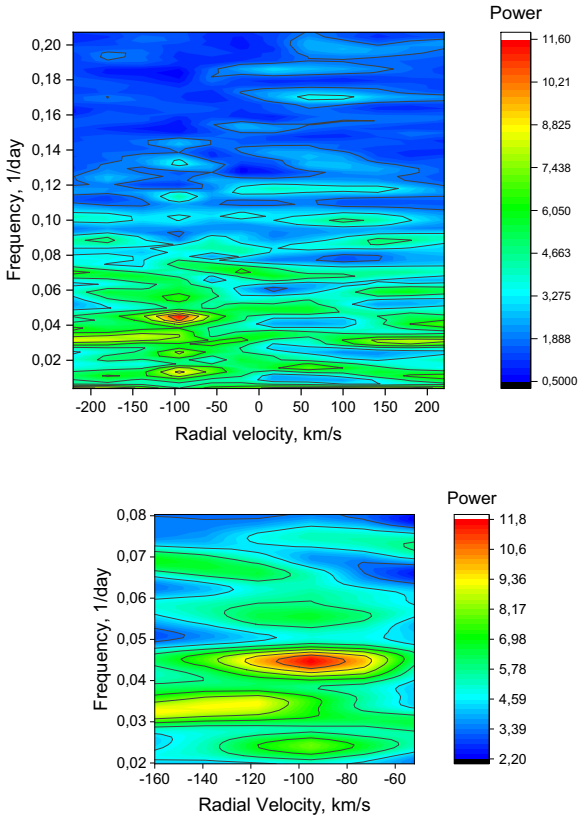

Figure 8. Upper: Two-dimensional periodogram of the H α line flux in RY Tau. Lower: Enlarged fragment of the periodogram. The red spot at RV = -95 ± 5 km s^{-1} indicates the area of the most powerful oscillations with a period of 21.6 d.

Periodic variations in the H α profile of RY Tau were previously reported in our publication, based on observations of 2013–2018: P = 21.6 d at RV = -100 km s^{-1} (Petrov et al. 2021). A similar analysis has been done using the whole set of data (9 seasons), corresponding to the years 2013–2022.

Fig. 8 shows a 2D periodogram of the H α flux variations in RY Tau. The most significant period is present at radial velocity -95 ± 5 km s^{-1}: the flux in this section of the profile varies with a period P = 21.6 d ($1/P = 0.0463$). The lower part of the Fig. 8 shows this region with better resolution.

The period is also present in the variations of the line profile asymmetry. In the case of RY Tau, the H α line profile is less regular,

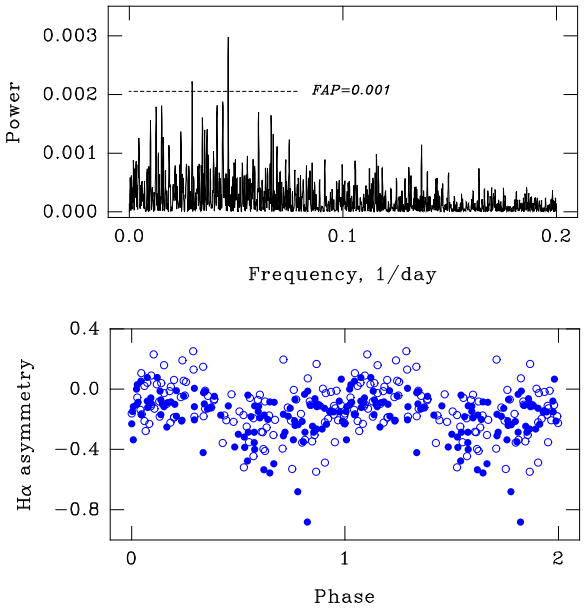

Figure 9. Top panel: Power spectrum of H α profile asymmetry in RY Tau. Bottom panel: H α profile asymmetry convolved with the period of 21.6 d. Dots and circles correspond to the first and the second halves of the time series, correspondingly.

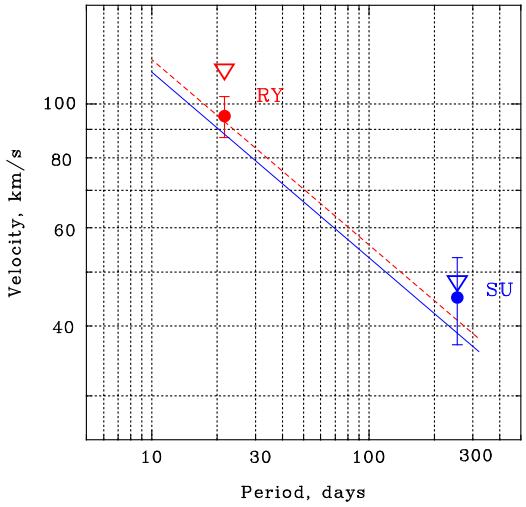

Figure 10. Two straight lines show the Keplerian relationship between the orbital velocity and the orbital period for the masses of RY Tau (red dashed line) and SU Aur (blue solid line). Dots with error bars show the observed radial velocities and periods in the H α flux variations in RY Tau and SU Aur. Open triangles indicate the deprojected radial velocities.

as compared to SU Aur: the position of the blue-shifted depression is not fixed at the same radial velocity, as well as the position of the red-shifted emission peak (see Fig. 7). Therefore, to measure the line asymmetry we use a more integrated parameter: $(b - r)/(b + r)$, where 'b' and 'r' are fluxes in the 'blue' and 'red' halves of H α profile, relative to zero radial velocity. The most negative values of the asymmetry correspond to the P Cyg type profile.

The power spectrum of H α line asymmetry and convolution of the asymmetry with the period of 21.6 d are shown in Fig. 9. About the same sinusoidal signal with the period of 21.6 d appears when the asymmetry of H α is expressed as the ratio of flux at radial velocity -95 km s^{-1} to the total flux in the line: $F_{-95}/F_{\rm total}$. The period of 21.6 d is also detected in the variability of the blue-shifted absorption of the D Na I lines, at a radial velocity of about -100 km s^{-1} (Petrov et al. 2021).

The level of false alarm probability FAP = 0.001, indicated in Figs 6 and 9, was estimated via the Fisher's Method of Randomization (Nemec & Nemec 1985). The highest peaks in the power spectra of SU Aur (Fig. 6) and RY Tau (Fig. 9) correspond to the 'red spots' in the 2D periodograms in Figs 5 and 8. In the case of RY Tau, the power spectrum shows two peaks above the FAP = 0.001. The less significant peak indicates variations with a period of about 34 d in the blue wing of H α emission. In the 2D periodogram (Fig. 8), it looks like a yellow strip at frequency $1/P \sim 0.03$, starting from RV $= -110$ km s^{-1}.

5 DISCUSSION

The light variations of SU Aur and RY Tau, observed during our spectroscopic monitoring (Figs 2 and 3), are typical for these stars. Taking into account the large inclination of the accretion discs, the short-term dimmings of SU Aur may be explained as a variable extinction in the dusty disc wind (Labdon et al. 2019). In RY Tau, the brightness variations over one magnitude can also be explained as due to circumstellar dust, because the veiling in the visible region of the photospheric spectrum remains low, < 0.1 (Petrov et al. 1999).

In both stars, RY Tau and SU Aur, the periodic changes appear in the blue wings of H α and the D Na I lines, in the radial velocities range that correspond to absorption in the wind. In the case of RY Tau, the period (21.6 d) could be assigned to the quasi-periodic outflows in the regime of the magnetic propeller. Therefore, in our previous publication (Petrov et al. 2021) we discussed two scenarios: (1) a stable magnetic propeller, or (2) a Keplerian motion of a planet at 0.2 au. In the case of SU Aur, the period is much longer and cannot be identified with the magnetic propeller regime. Therefore, we have to consider whether the periods are related to rotation in the accretion disc.

Accretion discs around CTTSs are expected to have magnetic fields, driving the disc wind out of the disc surface. The poloidal magnetic field lines diverge outwards due to the inward flow of matter in the disc plane and are twisted by the disc rotation. Thus, the ionized gas from the disc surface is accelerated into the wind by the magnetocentrifugal forces (Blandford & Payne 1982). Azimuthal asymmetries in the density distribution of the accretion disc lead to asymmetries in the wind.

The masses of RY Tau and SU Aur are known, so we can check whether the periods found are related to the Keplerian motion. In Fig. 10, the straight lines show the Keplerian relationship between the orbital velocity and the orbital period for the masses of RY Tau and SU Aur. The dots with error bars indicate the observed values of the periodic variations of the H α flux, and the radial velocities, at which these changes occur.

The spatial velocity of a gas particle in a disc wind may be considered as the sum of two vectors: toroidal and poloidal (e.g. Kurosawa et al. 2006). A gas particle starts from the surface of the disc and moves along an expanding spiral, rising above the disc plane. The blue-shifted absorption in the H α emission line profile is formed in the wind along the line of sight to the star. The observed radial velocity of this absorption is defined mainly by the wind acceleration in poloidal direction. The projection of the poloidal component to the line of sight depends on two angles: the inclination of the disc axis i, and the inclination of the wind stream to the disc

axis (the semi-open angle), which must be $\geq 30^{\circ}$ in order to start the centrifugal acceleration (Blandford & Payne 1982). Hence, the deprojected poloidal velocity: $V_{\rm p} \leq RV/\cos(i - 30)$. In Fig. 10, the estimated poloidal velocities of wind are shown with triangles.

In the magnetocentrifugal wind model, the terminal velocity of wind is proportional to the Keplerian velocity at the launching point on the accretion disc (Ferreira, Dougados & Cabrit 2006). In the case of high inclination i, the line of sight to the star crosses the wind streams launched from different radii in the disc plane. Assuming there is an axial asymmetry in the wind, caused by an azimuthal asymmetry in the structure of the accretion disc at a certain radius R_w, the column density of the disc wind on the line of sight to the star varies with a Keplerian period, corresponding to the orbital radius R_w.

The observed periodic changes in the disc wind do not yet mean the presence of a planet in the disc. Moreover, a planet by itself does not produce a density enhancement in the disc wind. There must be some feature in the accretion disc that rotates at Keplerian velocity and can create a non-axisymmetric dense structure in the wind.

What causes this asymmetry? Images of accretion discs of young stars obtained with the ALMA interferometer show that the surface brightness of the discs is significantly inhomogeneous, with different substructures, presumably reflecting different instabilities in the disc leading to maxima of gas pressure, or indicating the locations of planet formation (Andrews 2020).

Possible candidates for azimuthal asymmetry in the disc are vortices formed due to the Rossby wave instability (Lovelace et al. 1999; Li et al. 2000). They typically form in parts of the disc with a sharp density gradient, such as at the dead zone boundaries, dust sublimation radii, magnetospheric cavity boundary, or the edges of gaps opened by giant planets (e.g. Armitage & Kley 2019). A vortex represents the region of high pressure and density, which attracts dust particles. The vortex moves around a star approximately with a Keplerian velocity and rotates around the center of the vortex.

The derived orbital radius of 0.2 au in RY Tau is very close to the inner dusty disc radius of 0.2−0.3 au measured from near IR interferometry (e.g. Perraut et al. 2021) where some density jump is expected and vortices may form. Even higher density jump is expected at the inner dead zone transition (Gammie 1996), where the inner parts of the disc are strongly ionized and matter accretes more rapidly due to the MRI-driven turbulence (e.g. Balbus & Hawley 1991), while accretion rate is low in the external, weakly ionized parts of the disc. This density jump is shown to be a region where vortexes form (e.g. Varniere & Tagger 2006; Lyra & Mac Low 2012). The derived radii of 0.2−0.9 au for the location of the density enhancements in the disc are in the range of dead zones expected in considered stars. Simulations show that typically, the vortex is stable during many rotations (e.g. Li et al. 2001), however detailed radiative simulations by Faure et al. (2015) show that at the dead zone boundaries vortexes form episodically and migrate inwards in a cyclic manner. On average, the vortex position coincides with the location of the dead zone, and the period of azimuthal rotation will change if the dead zone will change its position.

If the vortex forms at the edge of the gap formed by a giant planet, then its period will be associated with a period of the planet and is expected to be more stable for a long time because a planet migrates slowly (see review by Armitage & Kley 2019). Periods obtained in our work can be connected with one of the above mechanisms.

Outflows from Rossby vortices are expected to have a higher density than those from surrounding parts of the disc and may produce a local stream of denser matter in the wind. The poloidal magnetic field threading the disc does not prevent the formation of Rossby vortices and driving matter into the wind (Yu & Lai 2013). Moreover, the rotation of the vortex leads to the generation of an additional, azimuthal magnetic field around the vortex which may contribute to driving denser matter into the wind (Lovelace & Romanova 2014; Matilsky et al. 2018).

The key condition for the stability of a stream of dense wind is the prevalence of magnetic pressure in the disc wind. There is the Alfven surface below which the magnetic pressure exceeds the gas pressure and the kinetic pressure: $B^2/8\pi > P_{\rm g} + \rho \cdot v^2$. Therefore, the streams of higher density in the wind cannot dissipate until they go above the Alfven surface. Below the Alfven surface, the disc wind 'remembers' the structure of the disc surface. This is a kind of magnetic 'memory' of the disc wind: it is permanently written at the base of the wind and erased above the Alfven surface.

These results open up new perspectives in studying the structure of the inner regions of the accretion discs. A method for mapping structural features on a moving surface, using changes in spectral line profiles, is known as the Doppler Imaging technique. It is widely applied in mapping spots on stars, where the inclination of the rotational axis and the period of rotation are well known. A similar technique, Doppler tomography, is applied for the analysis of the accretion disc emission-line regions in cataclysmic variables (Marsh & Horne 1988).

In the case of Classical T Tauri stars, by studying the density streams in the disc wind, we learn about the inner accretion disc structure and the orbital distances, related to planets formation. The method may be applied for the discs with high inclination, where the line of sight crosses the disc wind.

6 CONCLUSIONS

Spectroscopic monitoring of CTTS provides information about the gas flows around the stars. In the case of high inclination of the accretion disc, when the line of sight crosses the region of the disc wind below Alfven's surface, observations may reveal azimuthal asymmetry in the disc wind's density caused by the structural features of the disc surface. Our time series of RY Tau and SU Aur revealed stable periodic variations in the strength of the blue-shifted absorptions in H α and D Na I lines. The radial velocity of these variable absorptions, the periods of variations, and the masses of the stars are found to be related by Kepler's law. The structural details in the discs, presumably associated with Rossby waves, appeared at a distance of 0.2 au in RY Tau and 0.9 au in SU Aur. These findings open a possibility to research the structure of the inner accretion disc of a CTTS on scales of the order of one AU or less and to reveal the orbital distances, related to the formation of planets.

ACKNOWLEDGEMENTS

This work is partly based on observations made with the Nordic Optical Telescope, owned in collaboration by the University of Turku and Aarhus University, and operated jointly by Aarhus University, the University of Turku, and the University of Oslo, representing Denmark, Finland, and Norway, the University of Iceland and Stockholm University at the Observatorio del Roque de los Muchachos, La Palma, Spain, of the Instituto de Astrofisica de Canarias, using ALFOSC, which is provided by the Instituto de Astrofisica de Andalucia (IAA) under a joint agreement with the University of Copenhagen and NOT.

The Crimean observations in 2019–2020 by S. Artemenko, E. Babina, and P. Petrov were supported by a grant from the Russian Science Foundation 19-72-10063. The work of SYG was partially

supported by the Ministry of Science and Higher Education of Russia, topic no. FEUZ-2023-0019. MMR was supported in part by NSF grant AST-2009820. JFG was supported by fundação para a Ciência e Tecnologia (FCT) through the research grants UIDB/04434/2020 and UIDP/04434/2020.

We thank R. V. E. Lovelace for useful discussions and an anonymous referee for a thorough review that improved the paper.

DATA AVAILABILITY STATEMENT

The data underlying this article will be shared on reasonable request to the corresponding author [PP].

REFERENCES

Agra-Amboage V., Dougados C., Cabrit S., Garcia P. J. V., Ferruit P., 2009, A&A, 493, 1029
Akiyama E., Vorobyov E. I., Liu H. B., Dong R., de Leon J., Liu S.-Y., Tamura M., 2019, AJ, 157, 165
Alencar S. H. P. et al., 2018, A&A, 620, 195
Andrews S. M., 2020, ARA&A, 58, 483
Armitage P. J., Kley W., 2019, From Protoplanetary Disks to Planet Formation, Saas-Fee Advanced Course, Volume 45. Swiss Society for Astrophysics and Astronomy. Springer Berlin Heidelberg, Berlin
Artemenko S. A., Grankin K. N., Petrov P. P., 2012, AstL, 38, 783
Balbus S. A., Hawley J. F., 1991, ApJ, 376, 214
Blandford R. D., Payne D. G., 1982, MNRAS, 199, 883
Bouvier J., 1990, AJ, 99, 946
Bouvier J., Alencar S., Harries T., Johns-Krull C. M., Romanova M. M., 2007a, in Protostars and Planets V. Univ. Arizona Press, Tucson, p.479
Bouvier J. et al., 2007b, A&A, 463, 1017
Bouvier J. et al., 2023, A&A, 672, 5
Calvet N., Muzerolle J., Briceno C., Hernandez J., Hartmann L., Saucedo J. L., Gordon K. D., 2004, AJ, 128, 1294
Cody A. M., Tayar J., Hillenbrand L. A., Matthews J. M., Kallinger T., 2013, AJ, 145, 79
Davies C. L. et al., 2020, ApJ, 897, 31
DeWarf L. E., Sepinsky J. F., Guinan E. F., Ribas I., Nadalin I., 2003, ApJ, 590, 357
Faure J., Fromang S., Latter H., Meheut H., 2015, A&A, 573, 132
Ferreira J., Dougados C., Cabrit S., 2006, A&A, 453, 785
Gahm G. F., Gullbring E., Fischerstrom C., Lindroos K. P., Loden K., 1993, A&AS, 100, 371
Gammie C., 1996, ApJ, 457, 355
Garufi A. et al., 2019, A&A, 628, 68
Giampapa M. S., Basri G. S., Johns C. M., Imhoff C., 1993, ApJS, 89, 321
Ginski C. et al., 2021, ApJ, 908, 25
Grandjean A. et al., 2021, A&A, 650, 39
Grankin K. N., Melnikov S. Y., Bouvier J., Herbst W., Shevchenko V. S., 2007, A&A, 461, 183
Herbig G. H., Petrov P. P., Duemmler R., 2003, ApJ, 595, 384
Herbst W., Stine P. C., 1984, AJ, 89, 1716
Herbst W. et al., 1987, AJ, 94, 137
Herbst W., Herbst D. K., Grossman E. J., Weinstein D., 1994, AJ, 108, 1906
Isella A., Carpenter J. M., Sargent A. I., 2010, ApJ, 714, 1746
Ismailov N. Z., Adigezalzade A. N., Bahaddinova G. R., 2015, PKAS, 30, 229
Johns C., Basri G., 1995, AJ, 109, 2800
Kurosawa R., Romanova M. M., 2012, MNRAS, 426, 2901
Kurosawa R., Harries T. J., Symington N. H., 2006, MNRAS, 370, 580
Kurosawa R., Romanova M. M., Harries T. J., 2011, MNRAS, 416, 2623
Labdon A. et al., 2019, A&A, 561, 23
Li H., Finn J. M., Lovelace R. V. E., A. C. S., 2000, ApJ, 533, 1023
Li H., Colgate S. A., Wendroff B., Liska R., 2001, ApJ, 551, 874
Long F. et al., 2019, ApJ, 882, 49
Lovelace R. V. E., Romanova M. M., 2014, FlDyR, 46, 1401
Lovelace R. V. E., Li H., Colgate S. A., Nelson A. F., 1999, ApJ, 513, 805
Lyra W., Mac Low M.-M., 2012, ApJ, 756, 62
Marsh T., Horne K., 1988, MNRAS, 235, 269
Matilsky L., Dyda S., Lovelace R. V. E., Lii P. S., 2018, MNRAS, 480, 3671
Nemec A. F. L., Nemec J. M. A., 1985, AJ, 90, 2317
Nguyen D. C., Brandeker A., van Kerkwijk M. H., Jayawardhana R., 2012, ApJ, 745, 119
Nixon C. J., King A. R., Pringle J. E., 2018, MNRAS, 477, 3273
Pascucci I., Cabrit S., Edwards S., Gorti U., Gressel O., Suzuki T., 2023, in Inutsuka S.-i. Aikawa Y., Muto T., Tom K. Tamura M., eds, ASP Conf. Ser. Vol. 534, Protostars and Planets VII, Astron. Soc. Pac., San Francisco, p. 567
Percy J. R., Gryc W. K., Wong J. C. Y., Herbst W., 2006, PASP, 118, 1390
Perraut K. et al., 2021, The 20.5th Cambridge Workshop on Cool Stars, Stellar Systems, and the Sun (CS20.5), p. 334, http://coolstars20.cfa.harvard.edu/cs20half
Petrov P. P., Gullbring E., Ilyin I., Gahm G. F., Tuominen I., Hackman T., Loden K., 1996, A&A, 314, 821
Petrov P., Zajtseva G., Efimov Y., Duemmler R., Ilyin I. V., Tuominen I., Shcherbakov V. A., 1999, A&A, 341, 553
Petrov P., Gahm G. F., Stempels H. C., Walter F. M., Artemenko S. A., 2011, A&A, 535, 6
Petrov P. P. et al., 2019, MNRAS, 483, 132
Petrov P. P., Romanova M. M., Grankin K. N., Artemenko S. A., Babina E. V., Gorda S. Y., 2021, MNRAS, 504, 871
Powell S. L., Irwin M., Bouvier J., Clarke C. J., 2012, MNRAS, 426, 3315
Romanova M. M., Owocki S. P., 2015, SSRv, 191, 339
Romanova M. M., Ustyugova G. V., Koldoba A. V., Lovelace R. V. E., 2009, MNRAS, 399, 1802
Romanova M. M., Blinova A. A., Ustyugova G. V., Koldoba A. V., Lovelace R. V. E., 2018, NewA, 62, 94
S. Lawrence M. J., 1987, Digital Spectral Analysis with Applications. Prentice-Hall Signal Processing Series, Hoboken, New Jersey, U.S.
Shu F., Najita J., Ostriker E., Wilkin F., Ruden S., Lizano S., 2016, ApJ, 820, 139
Skinner S., Audard M., Guedel M., 2011, ApJ, 737, 19
Sousa A. P. et al., 2021, A&A, 649, 68
St-Onge G., Bastien P., 2008, ApJ, 674, 1032
Strassmeier K. G., Bartus J., Cutispoto G., Rodono M., 1997, A&AS, 125, 11
Tambovtseva L. V., Grinin V. P., Weigelt G., 2014, A&A, 562, 104
Varniere P., Tagger M., 2006, A&A, 446, 13
Xu Z., Herczeg G., Johns-Krull C., France C., 2021, ApJ, 921, 181
Yu C., Lai D., 2013, MNRAS, 429, 2748
Zajtseva G. V., 2010, Ap, 53, 212
Zajtseva G., Petrov P., Ilyin I., Duemler R., Tuominen I., 1996, IBVS, 4408, 1
Zanni C., Ferreira J., 2013, A&A, 550, 99
Zhu Z., Hartmann L., Calvet N., Hernandez J., Muzerolle J., Tannirkulam A.-K., 2007, ApJ, 669, 483

APPENDIX: OBSERVATION DATA

Table A1. RY Tau *V*-magnitudes for the dates of spectral observations in 2018–2022. The Heliocentric Julian Date (HJD) in the first column is followed by the site of the observation (CrAO – Crimean Astrophysical Observatory, UrFU – Kourovka astronomical observatory of Ural Federal University), magnitude measured in the *V* band, corresponding error and source (CrAO, AAVSO – American Association of Variable Star Observers, Int – value interpolated from AAVSO and CrAO phometry).

HJD-2400000	Site	*V*	*V* error	Source of *V*
58385.4814	CrAO	9.95	0.01	CrAO
58387.4837	CrAO	9.93	0.10	Int
58388.3744	CrAO	9.92	0.01	CrAO
58389.3881	CrAO	9.80	0.01	CrAO
58390.4398	CrAO	9.87	0.01	CrAO
58410.4249	CrAO	9.46	0.01	CrAO
58413.3276	CrAO	9.58	0.01	CrAO
58414.4158	CrAO	9.59	0.01	CrAO
58415.4108	CrAO	9.64	0.01	CrAO
58508.1821	CrAO	9.84	0.01	CrAO
58509.1849	CrAO	9.71	0.01	CrAO
58511.3288	CrAO	9.80	0.10	Int
58539.3164	CrAO	10.78	0.01	CrAO
58567.2115	CrAO	10.78	0.10	Int
58733.4181	CrAO	10.01	0.01	CrAO
58734.4325	CrAO	9.86	0.01	CrAO
58735.4190	CrAO	10.03	0.01	CrAO
58736.4114	CrAO	10.02	0.01	CrAO
58737.4201	CrAO	9.98	0.01	CrAO
58765.4148	CrAO	9.74	0.01	CrAO
58766.3949	CrAO	9.65	0.01	CrAO
58767.4075	CrAO	9.60	0.01	CrAO
58768.4256	CrAO	9.56	0.01	CrAO
58793.4984	CrAO	9.80	0.01	CrAO
58794.4122	CrAO	9.81	0.10	Int
58795.3102	CrAO	9.82	0.01	CrAO
58796.4116	CrAO	9.78	0.01	CrAO
58822.1974	CrAO	10.07	0.01	CrAO
58823.1794	CrAO	9.95	0.01	CrAO
58824.1764	CrAO	9.83	0.01	CrAO
58825.1786	CrAO	9.87	0.01	CrAO
58826.3344	CrAO	9.96	0.01	CrAO
58832.1747	CrAO	9.72	0.01	CrAO
58834.1948	CrAO	9.74	0.01	CrAO
58835.1767	CrAO	9.72	0.01	CrAO
58836.1848	CrAO	9.72	0.01	CrAO
58837.1782	CrAO	9.67	0.01	CrAO
59094.4484	CrAO	10.21	0.01	CrAO
59095.4479	CrAO	10.15	0.10	Int
59096.4027	CrAO	10.10	0.01	AAVSO
59118.4230	CrAO	10.09	0.10	Int
59119.4668	CrAO	10.09	0.01	CrAO
59120.3924	CrAO	10.10	0.01	CrAO
59121.4180	CrAO	10.10	0.01	CrAO
59123.4526	CrAO	10.24	0.01	AAVSO
59150.4246	CrAO	9.47	0.01	CrAO
59151.4660	CrAO	9.43	0.01	CrAO
59151.5010	UrFU	9.43	0.01	CrAO
59157.4042	UrFU	9.50	0.10	Int
59174.3277	CrAO	9.70	0.10	Int
59176.4235	CrAO	9.73	0.01	CrAO
59178.4348	CrAO	9.77	0.01	CrAO
59189.1893	CrAO	10.27	0.01	CrAO
59190.2879	CrAO	10.03	0.01	CrAO
59194.4090	UrFU	9.75	0.10	Int
59195.4826	UrFU	9.73	0.10	Int
59203.5020	UrFU	9.54	0.10	Int
59217.1873	CrAO	9.66	0.01	CrAO
59221.1563	CrAO	9.72	0.01	CrAO
59251.1820	CrAO	10.01	0.01	CrAO
59278.2196	CrAO	9.89	0.01	CrAO
59279.2029	CrAO	9.94	0.01	CrAO
59280.2914	CrAO	9.95	0.10	Int
59288.2045	CrAO	9.94	0.01	CrAO
59475.4156	CrAO	10.00	0.10	Int
59477.4852	CrAO	9.96	0.01	CrAO
59505.4315	CrAO	10.28	0.01	CrAO
59508.3752	CrAO	10.28	0.01	CrAO
59531.2225	CrAO	10.44	0.01	CrAO
59532.2283	CrAO	10.65	0.01	AAVSO
59533.2331	CrAO	10.67	0.10	Int
59534.2230	CrAO	10.69	0.01	CrAO
59544.2192	CrAO	10.37	0.01	CrAO
59545.2085	CrAO	10.30	0.10	Int
59586.3711	CrAO	10.10	0.10	Int
59599.3919	CrAO	10.30	0.10	Int
59624.1807	CrAO	10.38	0.01	CrAO
59632.2225	CrAO	9.94	0.01	CrAO
59652.2014	CrAO	10.03	0.01	CrAO
59654.2259	CrAO	10.23	0.01	CrAO
59663.2065	CrAO	9.76	0.01	CrAO
59665.2201	CrAO	9.72	0.01	CrAO
59666.2159	CrAO	9.77	0.01	CrAO

Table A1 – *continued*

Table A2. SU Aur *V*-magnitudes for the dates of spectral observations in 2018–2022. The Heliocentric Julian Date (HJD) in the first column is followed by the site of the observation (CrAO – Crimean Astrophysical Observatory, UrFU – Kourovka astronomical observatory of Ural Federal University), magnitude measured in the *V* band, corresponding error and source (CrAO, AAVSO – American Association of Variable Star Observers, Int – value interpolated from AAVSO and CrAO phometry).

HJD-2400000	Site	*V*	*V* error	Source of *V*
58385.5254	CrAO	9.35	0.01	CrAO
58387.5306	CrAO	9.55	0.01	CrAO
58388.4419	CrAO	9.33	0.01	CrAO
58389.4523	CrAO	9.36	0.01	CrAO
58390.5045	CrAO	9.40	0.01	CrAO
58410.4894	CrAO	9.34	0.01	CrAO
58413.3925	CrAO	9.32	0.01	CrAO
58414.4808	CrAO	9.35	0.01	CrAO
58415.4753	CrAO	9.34	0.01	CrAO
58508.2357	CrAO	9.53	0.01	CrAO
58509.2595	CrAO	9.50	0.01	CrAO
58511.3531	CrAO	9.40	0.10	Int
58521.3400	UrFU	9.35	0.10	Int
58535.2368	UrFU	9.51	0.01	CrAO
58539.2519	CrAO	9.44	0.01	CrAO
58559.2333	UrFU	9.62	0.02	AAVSO
58567.2619	CrAO	9.60	0.10	Int
58568.2508	CrAO	9.52	0.01	CrAO
58733.4841	CrAO	9.40	0.01	CrAO
58734.4970	CrAO	9.44	0.01	CrAO
58735.4834	CrAO	9.34	0.01	CrAO
58736.4770	CrAO	9.26	0.01	CrAO
58737.4841	CrAO	9.27	0.01	CrAO
58765.4834	CrAO	9.32	0.01	CrAO
58766.4600	CrAO	9.33	0.01	CrAO
58767.4518	CrAO	9.29	0.01	CrAO
58768.4906	CrAO	9.34	0.01	CrAO
58793.4281	CrAO	9.27	0.10	Int

Table A2 – *continued*

HJD-2400000	Site	*V*	*V* error	Source of *V*
58794.4564	CrAO	9.28	0.01	CrAO
58795.3754	CrAO	9.29	0.01	CrAO
58796.4773	CrAO	9.24	0.01	CrAO
58822.2870	CrAO	9.34	0.01	CrAO
58823.2465	CrAO	9.25	0.01	CrAO
58824.2414	CrAO	9.29	0.01	CrAO
58825.2342	CrAO	9.28	0.01	CrAO
58826.3785	CrAO	9.27	0.01	CrAO
58832.2412	CrAO	9.27	0.01	CrAO
58834.2621	CrAO	9.26	0.01	CrAO
58835.2633	CrAO	9.24	0.01	CrAO
58836.2718	CrAO	9.23	0.01	CrAO
58837.2858	CrAO	9.21	0.01	CrAO
58847.3812	UrFU	9.32	0.10	Int
58851.2413	CrAO	9.36	0.01	CrAO
58862.3010	CrAO	9.26	0.01	CrAO
58864.2685	CrAO	9.24	0.01	CrAO
58865.2706	CrAO	9.25	0.01	CrAO
58877.2560	UrFU	9.27	0.01	Int
58889.3070	CrAO	9.41	0.01	CrAO
58890.2680	CrAO	9.45	0.01	CrAO
58914.2987	UrFU	9.55	0.10	Int
58916.2893	CrAO	9.51	0.01	CrAO
58918.2852	CrAO	9.37	0.01	CrAO
58923.2899	CrAO	9.35	0.01	CrAO
58925.2692	CrAO	9.55	0.01	CrAO
58926.2454	CrAO	9.63	0.01	CrAO
58932.2576	UrFU	9.60	0.10	Int
58936.2847	UrFU	9.60	0.10	Int
59094.5135	CrAO	9.45	0.01	CrAO
59095.5174	CrAO	9.47	0.10	Int
59096.4822	CrAO	9.50	0.10	Int
59119.5152	CrAO	9.86	0.01	CrAO
59120.4622	CrAO	10.00	0.01	CrAO
59121.4901	CrAO	10.03	0.01	CrAO
59150.5046	CrAO	9.50	0.01	CrAO

Table A2 – *continued*

HJD-2400000	Site	*V*	*V* error	Source of *V*
59151.4993	UrFU	9.56	0.01	CrAO
59151.5310	CrAO	9.56	0.01	CrAO
59174.3962	CrAO	9.64	0.10	Int
59176.4926	CrAO	9.65	0.01	CrAO
59189.2371	CrAO	9.58	0.01	CrAO
59190.3823	CrAO	9.64	0.01	CrAO
59217.2541	CrAO	9.68	0.01	CrAO
59218.2252	CrAO	9.68	0.01	CrAO
59219.2124	CrAO	9.70	0.01	CrAO
59221.2569	CrAO	9.83	0.01	CrAO
59249.2494	CrAO	9.40	0.01	CrAO
59257.3505	UrFU	9.33	0.10	AAVSO
59275.3060	UrFU	9.36	0.10	Int
59279.2716	CrAO	9.34	0.01	CrAO
59287.2796	UrFU	9.34	0.10	Int
59288.2700	CrAO	9.35	0.01	CrAO
59288.2886	UrFU	9.35	0.01	CrAO
59296.2526	UrFU	10.03	0.10	AAVSO
59318.2247	UrFU	9.90	0.10	Int
59477.5286	CrAO	9.72	0.01	CrAO
59505.4855	CrAO	9.55	0.01	CrAO
59533.2996	CrAO	9.50	0.10	Int
59544.3023	CrAO	9.73	0.01	CrAO
59586.4188	CrAO	9.60	0.10	Int
59598.2719	CrAO	9.58	0.01	CrAO
59599.4372	CrAO	9.58	0.10	Int
59624.2683	CrAO	9.53	0.01	CrAO
59628.2886	CrAO	9.49	0.01	CrAO
59630.2814	CrAO	9.45	0.10	Int
59632.2727	CrAO	9.38	0.01	CrAO
59652.2676	CrAO	9.44	0.01	CrAO
59663.2538	CrAO	9.43	0.01	CrAO
59665.2656	CrAO	9.43	0.01	CrAO
59666.2610	CrAO	9.55	0.01	CrAO
59667.2560	CrAO	9.53	0.01	CrAO

This paper has been typeset from a TEX/LATEX file prepared by the author.